

Effect of Structural Parameter on Superconductivity of Iron-Based Superconductor $\text{FeSe}_{1-x}\text{Te}_x$

By systematic crystal structure refinements of characteristic superconductor, $\text{FeSe}_{1-x}\text{Te}_x$ ($x = 0.5, 0.625, 0.75, 0.875$) and FeSe by the powder neutron diffraction technique, we studied the relationship between crystal structure and superconductivity. In this work, we found the role of Fe-X network (X; calcogens, pnictogens,) for the mechanism of the iron-based superconductor. This work is a result of collaboration investigations between IMR and WPI-AIMR groups.

The discovery of superconductivity in the iron oxypnictide family of compounds has generated considerable interest in the mechanism of superconductivity.[1] The understanding of electronic, magnetic and structural properties of these compounds is the key to elucidation of this mechanism. Lee *et al.* have reported that T_c becomes maximum when FeAs_4 -lattices form a regular tetrahedron (As-Fe-As angle $\alpha = 109.47^\circ$).[2] This result indicates a relationship between crystal structure and superconductivity. However, it has not been clarified whether this relationship is a universal feature of the iron superconductor because there are only a few reports on the crystal structure analysis of materials with lower α angle ($\alpha > 105^\circ$). Recently, superconductivity was discovered in $\alpha\text{-FeSe}_x$ system. The crystal structure of FeSe is the most simplest, and the Se-Fe-Se angle of FeSe_4 -tetrahedra at $\sim 105^\circ$ is considerably smaller than that of the iron oxypnictide family. Therefore, we attempt to determine the crystal structural parameters of $\text{FeSe}_{1-x}\text{Te}_x$ by using the neutron diffraction technique.

We performed neutron powder diffraction experiments on the Kinken powder diffractometer for high efficiency and high resolution measurements, HERMES, of Institute for Materials Research, Tohoku University, installed at the JRR-3 reactor in Japan Atomic Energy Agency, Tokai.

The relationship between T_c and X-Fe-X (X=As, P, Se

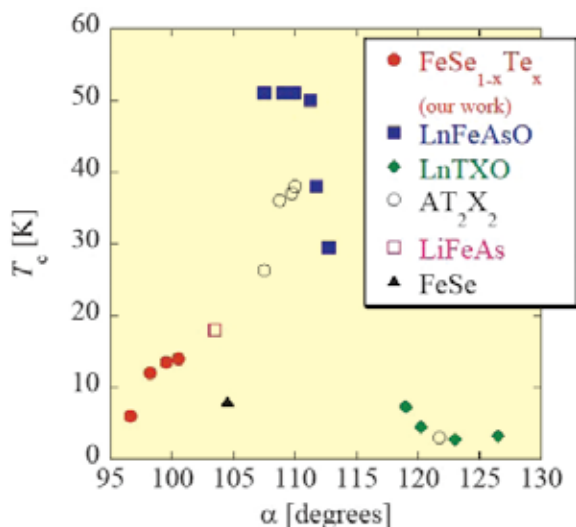


Fig. 1 X-Fe-X (X:As, P, Se and Te) angle α dependence of superconducting transition temperature T_c .

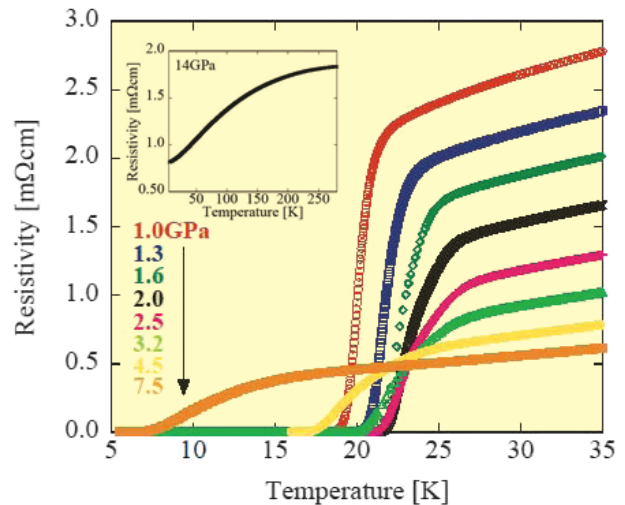


Fig. 2 Superconducting transition in $\text{FeSe}_{0.5}\text{Te}_{0.5}$ under high pressures. Inset shows the temperature dependence of electrical resistivity under 14GPa.

and Te) angle is shown Fig.1. The T_c of the $\text{FeSe}_{1-x}\text{Te}_x$ system increases with increasing α , indicating that this relationship is universal feature and crystal structure plays an important role in the iron superconductor.

From the structural analysis, $\text{Fe}(\text{Se},\text{Te})_4$ -tetrahedrons distort greatly from the regular shape implies the improvement of T_c upon applying pressure. Thus, we have performed on the high-pressure resistivity experiments in $\text{FeSe}_{0.5}\text{Te}_{0.5}$, which shows the maximum $T_c (=14\text{K})$ under ambient pressure. Figure 2 shows the temperature dependence of the resistivity of $\text{FeSe}_{0.5}\text{Te}_{0.5}$ at various pressure up to 7.5GPa. The onset temperature of T_c increases rapidly from 14K to 26K applying up to 2GPa and the metallic phase was observed at $P=14\text{GPa}$. This experiment presents the first observation of a phase transition from a superconducting to metallic phase on the P - T_c phase diagram.[3]

This work has been selected as Editor's choice Paper of J. Phys. Soc. Jpn. in 2009.

References

- [1] Y. Kamihara et al., J. Am. Chem. Soc. **130** (2008) 3296.
- [2] C. H. Lee et al., J. Phys. Soc. Jpn. **77** (2008) 083704.
- [3] K. Horigane et al., to be published in JPSJ

Key Words

Superconductivity, Structural Effect, Neutron Diffraction

Contact to

Kenji Ohoyama (Metal Physics with Quantum Beam Spectroscopy Division)
e-mail: ohoyama@imr.tohoku.ac.jp

Theoretical Research for Improved Hydrogen Storage Materials

Hydrogen is attractive as a fuel because its use creates neither air pollution nor greenhouse-gas emissions. The use of hydrogen requires an effective, safe, and stable storage medium. However, how to store hydrogen easily and cheaply is still a challenging problem. The current methods of storing hydrogen as compressed gas or in the liquid form do not meet the industrial requirements because the energy densities are much lower than that in gasoline. Moreover, there are issues of safety and cost involved in compressing hydrogen under high pressure or liquefying it at cryogenic temperatures. Although storage of hydrogen in solid-state materials offers an alternative, there are no current solid-state storage materials that meet the industry requirements. Doping of transition and alkali elements increases the hydrogen storage capacity of many materials. Inspired by these finds, we explore the hydrogen storage properties of transition metal doped boron nitride sheets, lithium doped Metal Organic Frameworks (MOFs) and Lithium doped calix[4]arenes. All the numerical calculations have been conducted by using the HITACHI SR11000 K2/51 supercomputing system at the Center for Computational Materials Science, IMR.

Theoretical calculation shows that BN sheets storage capacity can be improved from > 1 to over 2.5 wt.% by doping with transition metal atoms (Ni and Rh). The site of metal doping was found to play a major role in the capacity of hydrogen storage. Both Ni and Rh atoms are capable to absorb up to three hydrogen molecules chemically and the metal atom to BN sheet distance increases with the increase in the number of hydrogen molecules. Our calculations offer explanation for the nature of bonding between the metal atom and the hydrogen molecules, which is due to the hybridization of metal d orbital with the hydrogen s orbital [1].

Li adsorption on isorecticular MOFs with metal Fe, Cu, Co, Ni and Zn was studied using density function theory. Li functionalization shows a considerable structural change associated with a volume change in isorecticular MOF-5 except for the Zn metal center. Hydrogen binding energies on Li functionalized MOFs are seen to be in the range of 0.2 eV, which is the desired value for an ideal reversible storage system. Each Li atom doped was found to hold three H₂ molecules firmly due to the charge induced dipole interaction. The most stable position for Li atom was found was on the benzene ring, This study has clearly shown that Li doping is possible only in Zn-based MOF-5, which would be better candidate to reversibly store hydrogen [2].

Density functional theory (DFT) was performed to investigate hydrogen storage in Li-functionalized p-tert-butyl

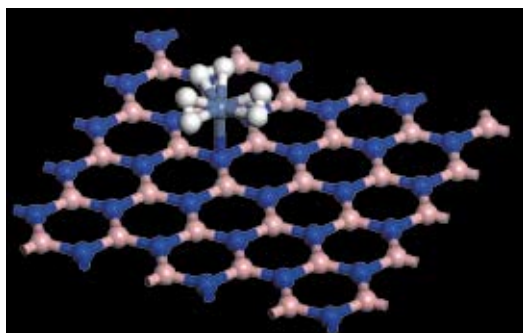


Fig. 1 Optimized geometric structures for the hydrogen adsorbed on the metal doped BN sheet.

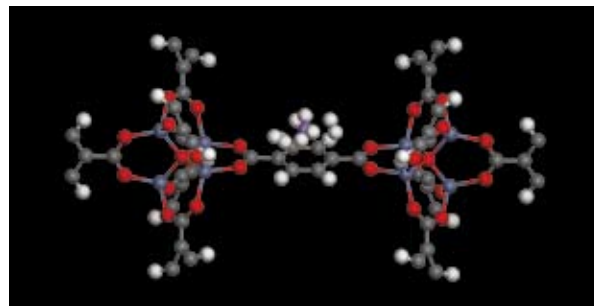


Fig. 2 Optimized geometries of adsorbed hydrogen molecules on Li functionalized Zn-MOF-5 with four hydrogen molecules.

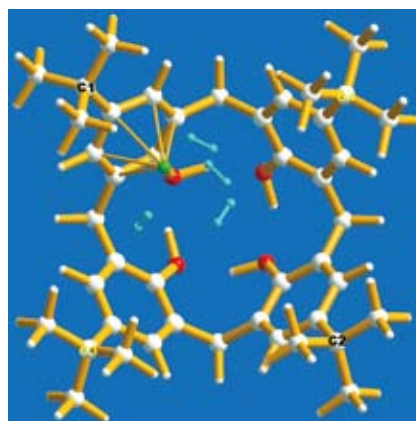


Fig. 3 Optimized geometries for Li-functionalized calixarene with four hydrogen molecules.

calixarene (LTBC). The pure organic compound, *p*-tert-butylcalix[4]arene (TBC), has the capability to store hydrogen up to 0.6 wt.%. TBC was found to hold one H₂ molecules inside its cavity and the Li-functionalized calixarene was able to hold 4 H₂ molecules inside its cavity. Calculations based on DFT show that Li-functionalized calixarene significantly improves the average binding energy of hydrogen molecules. The mean distance between the Li and hydrogen molecules increases with the increase in the number of hydrogen molecules. *Ab initio* molecular dynamic studies show that Li-functionalized TBC is stable up to 200K while hydrogen incorporated material was stable up to 100K [3].

References

- [1] N. S. Venkataramanan, M. Khazaei, R. Sahara, H. Mizuseki, and Y. Kawazoe, *Chem. Phys.* **359** (2009) 173-178.
- [2] N. S. Venkataramanan, R. Sahara, H. Mizuseki, and Y. Kawazoe, *Int. J. Mol. Sci.* **10** (2009) 1601-1608.
- [3] N. S. Venkataramanan, R. Sahara, H. Mizuseki, and Y. Kawazoe, *J. Phys. Chem. C.* **112** (2008) 19676-19679.

Key Words

Hydrogen Storage Material, First Principles Calculations, Metal Organic Frameworks

Contact to

Yoshiyuki Kawazoe (Materials Design by Computer Simulation Division)
e-mail: kawazoe@imr.edu

Aluminum Hydride for Hydrogen Storage

Hydrogen desorption reaction of aluminum hydride, AlH_3 , was investigated by *in situ* microscopic observations combined with thermal and surface analyses. Before the hydrogen desorption reaction, primary AlH_3 particles of size 100 nm–1 μm were thought to be covered by an oxide layer with a thickness of less than 5 nm. The morphologies of the particles covered by the layer did not change during the hydrogen desorption reaction.

Complex hydrides with high hydrogen density are being extensively studied for developing advanced hydrogen storage materials [1]. Aluminum trihydride (AlH_3 , alane) also has high gravimetric and volumetric hydrogen densities (10 mass% and 149 kgH_2/m^3 , respectively). Equilibrium hydrogen pressure of $\alpha\text{-AlH}_3$ (the most stable phase among the variants of the crystalline structure) is around 1 GPa at 298 K, although AlH_3 undergoes a simple hydrogen desorption reaction ($\text{AlH}_3 \rightarrow \text{Al} + 3/2\text{H}_2$) at 370–470 K [2].

Fig. 1 shows the TG profile and SEM images during the hydrogen desorption reaction of the AlH_3 particles [3]. The TG profile shows that the hydrogen desorption reaction starts at approximately 370 K and the amount of desorbed hydrogen is 9.6 ± 0.2 mass% (corresponding to 96% of the ideal amount in AlH_3 , 10.1 mass%). From the XRD profiles, we confirmed the existence of single-phase $\alpha\text{-AlH}_3$ with a molecular volume of $33.4 \text{ \AA}^3/\alpha\text{-AlH}_3$ and metallic Al with a molecular volume of $16.6 \text{ \AA}^3/\text{Al}$ before and after the hydrogen desorption reaction, respectively. The two-fold shrinkage in molecular volume from $\alpha\text{-AlH}_3$ to metallic Al was highly expected to cause a change in the morphologies of the primary particles. The SEM images, however, indicate that the morphologies of the particles of size 100 nm–1 μm do not change at all during the hydrogen desorption reaction, as shown in Figs. 1 (a) – (c).

A TEM image of the primary AlH_3 particles before the hydrogen desorption reaction is shown in Fig. 2 (a) [3]. Electron diffraction patterns suggested that the particles before the hydrogen desorption reaction are single crystals of $\alpha\text{-AlH}_3$. In addition, electron energy-loss spectroscopy and X-ray photoelectron spectroscopy revealed that the primary AlH_3 particles are covered by a surface layer of amorphous aluminum oxide with a thickness of 3–5 nm [3, 4].

Furthermore, the TEM images taken during the hydrogen desorption reaction (heating achieved by electron irradiation) are shown in Figs. 2 (b) and (c). Clearly, nanoscale (~1 nm) precipitations can be observed inside the primary AlH_3 particles of size 100–200 nm; then, these precipitations exhibit a continuous grain-growth (20–50 nm). Simultaneously, the 'boundary space' in the primary AlH_3 particles increases because of the shrinkage in the molecular volume from $\alpha\text{-AlH}_3$ to metallic Al, as described above. The electron diffraction pattern indicates the existence of polycrystalline metallic Al after the hydrogen desorption reaction; it may be noted that the polycrystals were formed from a single crystal of AlH_3 during the hydrogen desorption reaction. On the surface layer, neither the formation of cracks nor a change in thickness was observed during the hydrogen desorption reaction. It was, therefore, found that the surface morphology of the primary AlH_3 particles was not affected by the hydrogen desorption reaction; however, the nanostructure inside the particles was found to change drastically because of the precipitation and continuous grain-growth of metallic Al. Thus, the surface layer on the primary AlH_3 particles should

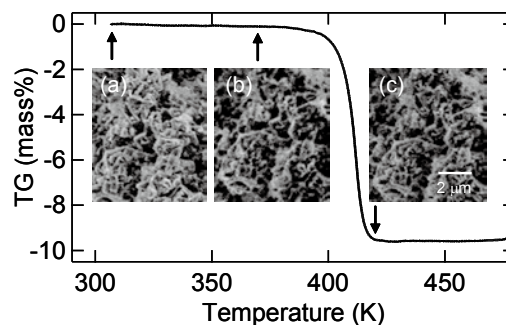


Fig. 1 Thermogravimetry (TG) profile and *in situ* SEM images of the AlH_3 particles [3]. (a) before the hydrogen desorption reaction, and during the reaction at (b) 370 K and (c) 420 K.

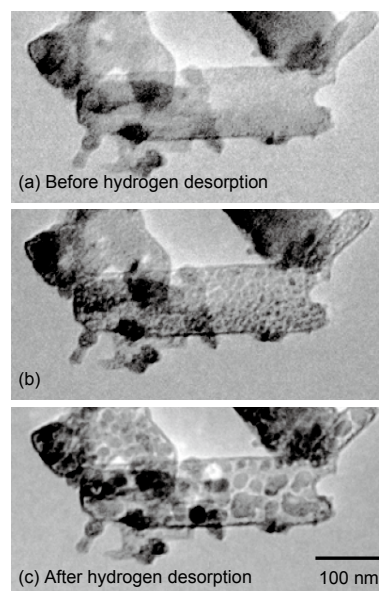


Fig. 2 TEM images of the primary AlH_3 particles (a) before, (b) during and (c) after the hydrogen desorption reaction [3].

play a dominant role against the occurrence of the hydrogen desorption reaction (thereby retaining the ' AlH_3 ' structure inside the particles) at room temperature.

References

- [1] S. Orimo, Y. Nakamori, J.R. Eliseo, A. Züttel and C.M. Jensen, *Chem. Rev.* **107**, 4111 (2007).
- [2] S. Orimo, Y. Nakamori, T. Kato, C. Brown and C.M. Jensen, *Appl. Phys. A* **83**, 5 (2006).
- [3] K. Ikeda, S. Muto, K. Tatsumi, M. Menjo, S. Kato, M. Biemann, A. Züttel, C.M. Jensen and S. Orimo, *Nanotechnology* **20**, 204004 (2009).
- [4] S. Muto, K. Tatsumi, K. Ikeda and S. Orimo, *J. Appl. Phys.* **105**, 123514 (2009).

Key Words

Aluminum Hydride, Hydrogen Storage Material, Transmission Electron Microscope Observation

Contact to

Kazutaka Ikeda (Hydrogen Functional Materials Division)
e-mail: kikeda@imr.tohoku.ac.jp

Multiple Superior Properties of New Au-based Bulk Glassy Alloys with Ultralow Glass Transition Temperature

New Au-based Au-Cu-Ag-Si bulk glassy alloys (BGAs) with high Au contents exhibit ultralow glass transition temperature (T_g), high glass-forming ability (GFA), wide supercooled liquid region (ΔT_x), good mechanical properties, excellent corrosion resistance, high thermodynamic and kinetic stability in supercooled liquid state, strong oxidation resistance, and excellent thermoplastic formability[1].

The Au-based BGAs contain high Au content of ~70 at.% (89 wt.%), which is much higher than that of 18-karat Au. The alloys show wide ΔT_x of ~36-50 °C and ultralow T_g of ~ 66 -102 °C (see Fig.1), which is the lowest in the T_g among known BGAs except Ca-based alloys. The alloys also possess high GFA, and the full glassy sample diameters are in the range of ~2-5 mm. The glassy alloys can be prepared by melt spinning and copper mold casting in air. Their luster and thermal properties are the same as those of the samples prepared in an argon atmosphere, indicating the strong oxidation resistance even at high temperature, which is similar to gold.

Although the Au-based BGAs show ultralow T_g , they have high stability at ambient temperatures. These BGAs stored at room temperature (RT) for more than 4 months are still in a fully glassy state. Their stability is also testified by temperature-time-transformation (TTT) diagram shown in Fig. 2. Arrhenius extrapolation with a predicted lifetime at RT (20°C) is over of 4.9×10^7 s. It is estimated that the fully glassy state can be kept at RT for at least 18 months.

Mechanical tests on these BGAs exhibit quite high compressive fracture strength of ~ 643-935 MPa, Young's modulus of ~ 46.6-65.4 GPa and high Vicker's hardness of ~ 264-353. Their corrosion resistance in 1N HCl and 1N H₂SO₄ solutions is similar to that of Ni-based BGAs, and much better than those of other BGAs and SUS316L.

The Au-based BGAs have low viscosity of ~ 10^7 Pa.s in the supercooled liquid state, making them easy to deform thermoplastically at a temperature below 100°C. Figure 3 (a) shows the glassy rods formed into U shapes by using two pairs of tweezers in near-boiling water. A small dish shape (Fig. 3 (b)) is pressed from a glassy plate using a pair of pliers. The pattern on the surface is copied from the engaging teeth of the pliers. It has been demonstrated that the glassy pillars with nanoscale diameters can be formed directly by imprinting. Fig. 3 (c) shows SEM image of glassy pillars with diameters of about 200 nm fabricated by isothermal processing of Au₆₀Cu_{15.5}Ag_{7.5}Si₁₇ alloy on porous alumina at 92 °C for 180

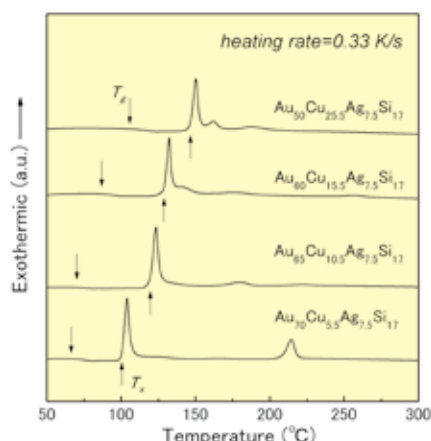


Fig. 1 DSC curves of Au₅₀₋₇₀Cu_{5-25.5}Ag_{7.5}Si₁₇ glassy alloys.

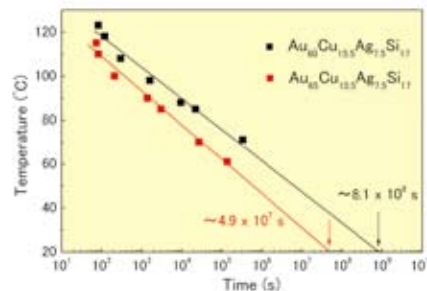


Fig. 2 TTT diagrams of Au₆₀Cu_{15.5}Ag_{7.5}Si₁₇ and Au₆₅Cu_{10.5}Ag_{7.5}Si₁₇ glassy alloys. The solid lines extrapolated to RT (~20°C) show their onset time for crystallization at RT are 8.1×10^8 and 4.9×10^7 s, respectively.

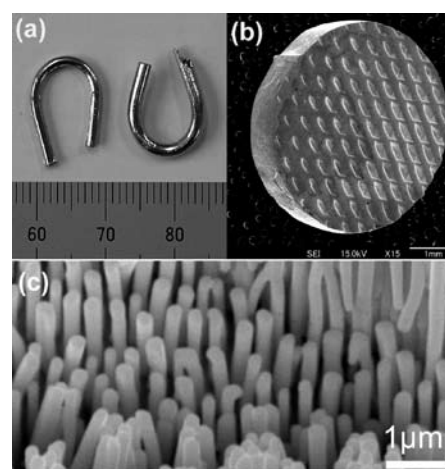


Fig. 3 (a) Au₆₀Cu_{15.5}Si₁₇Ag_{7.5} glassy rods formed into U shapes by using two pairs of tweezers in near-boiling water (97°C). (b) Pattern formed by a pair of pliers on the surface of the glassy plate ($\Phi 5 \times 1.5$ mm²) in near-boiling water. (c) SEM image of the nano-glassy pillars formed by imprinting on porous alumina. The pillars with diameters of about 200 nm are formed when the alloy is heated through its supercooled liquid region (92°C) for 180 s under an applied pressure of 100 MPa.

s under an applied pressure of 100 MPa. The results indicate that the shaping, imprinting and other thermoplastics processes can be conveniently applied to the BGAs.

The combination of the many superior properties makes the new Au-based BGAs excellent prospects for scientific and many applications, including micro/nano-machinery, bioengineering, high density data recording media, and jewelry.

References

[1] W. Zhang, H. Guo, M. W. Chen, Y. Saotome, C. L. Qin and A. Inoue, Scripta. Mater, 61 (2009) on line.

Key Words

Metallic Glass, Glass Transition Temperature, Thermoplastic Formability

Contact to

Wei Zhang (Research and Development Project on Advanced Metallic Glasses, Inorganic Materials and Joining Technology) e-mail: wzhang@imr.tohoku.ac.jp

Development of the Ni-based Metallic Glassy Bipolar Plates for Proton Exchange Membrane Fuel Cell (PEMFC)

The $Ni_{65}Cr_{15}P_{16}B_4$ glassy alloy was found to be an optimal alloy for bipolar plate of PEMFC. A bipolar plate was successfully produced by hot-pressing the glassy alloy sheet in a supercooled liquid state. The I-V characteristics of a single cell with the glassy bipolar plates were measured.

Proton exchange membrane (PEM) fuel cells have been receiving considerable attention as clean energy sources that may be used in the near future. Bipolar plates are conventionally made of carbon graphite. However, it cannot be used to produce thin bipolar plates because of its brittleness. Thinner bipolar plates will result in lighter and more compact fuel cell stacks, saving costs and enhancing the usefulness of fuel cells.

Recently, many research groups have tried to develop metallic materials for bipolar plates. The corrosion-resistant stainless steel SUS316L is recognized as a standard material for comparison. Many different types of metallic bipolar plates have subsequently been developed, including those based on stainless steels or other alloys with coatings.

Metallic glassy alloys are also potential materials for bipolar plates because they have many advantageous characteristics over crystalline alloys [1, 2]. For example, glassy alloys exhibit higher mechanical strengths and higher corrosion resistance. Furthermore, metallic glasses can show viscous flow (plastic) deformation in a supercooled liquid state at temperatures between the glass transition temperature, T_g , and the crystallization temperature, T_x .

Recently, we found that a Ni-Cr-P-B glassy alloy could be melt-spun even in air without any degradation in its thermal or other properties and that it had a wide supercooled liquid region ΔT_x .

In this work, we adopted the above mentioned Ni-Cr-P-B quaternary system and optimized the alloy compositions suitable for bipolar plate production. After the screening, the $Ni_{65}Cr_{15}P_{16}B_4$ metallic glass was selected in this study as an optimal alloy having as wider ΔT_x , and lower T_g and T_x as

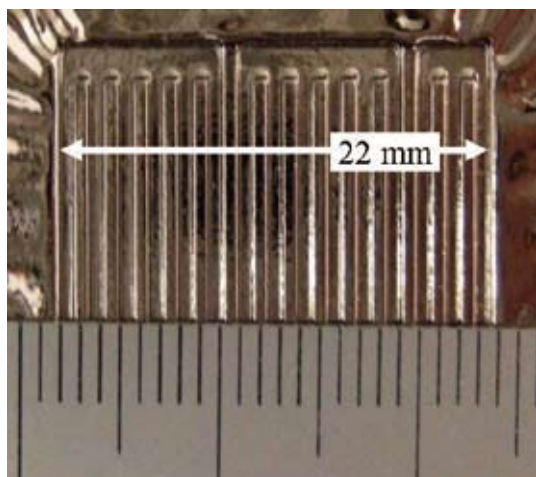


Fig. 1 Optical micrograph of the $Ni_{65}Cr_{15}P_{16}B_4$ glassy alloy bipolar plate produced by hot-pressing in the super-cooled liquid state.

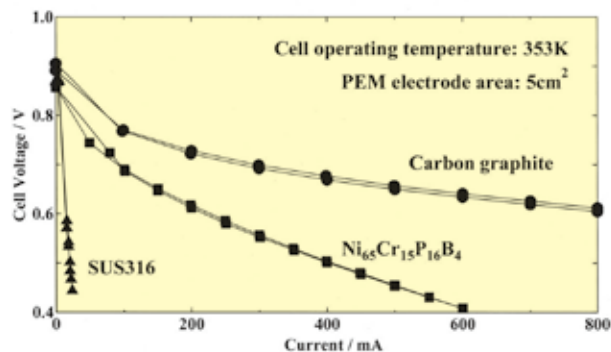


Fig. 2 Comparison of I-V characteristics between cells with $Ni_{65}Cr_{15}P_{16}B_4$ glassy alloy bipolar plates and SUS316 plates.

possible. The T_g , T_x and ΔT_x of the $Ni_{65}Cr_{15}P_{16}B_4$ glassy alloy are 659 K, 702 K and 43 K, respectively. A bipolar plate was then produced by hot-pressing in a supercooled liquid state. Finally the I-V characteristics were tentatively obtained for the glassy alloy.

Figure 1 shows a bipolar plate produced by hot-pressing the $Ni_{65}Cr_{15}P_{16}B_4$ glassy alloy sheet at 679 K ($=T_g+20$ K) for 300 s in a dilute Ar atmosphere in the supercooled liquid state. The groove depth is 0.7 mm. Excellent viscous flow deformation was obtained as clearly demonstrated in this figure.

Figure 2 indicates the I-V curves of single cells with $Ni_{65}Cr_{15}P_{16}B_4$ glassy and SUS316 bipolar plates. The as-processed glassy plates were used for these measurements without any further surface-treatment. The SUS316 bipolar plates were produced by machining. The same flow field design was adopted for both bipolar plates. The metallic glassy bipolar plates were mounted on a carbon frame and used for measurement. In the potentiodynamic corrosion tests, the current density of the non-polished Ni-Cr-P-B sample is smaller than that of the SUS316L alloy. This is also reflected in the better performance of the single cell with $Ni_{65}Cr_{15}P_{16}B_4$ glassy plates. However, the carbon bipolar plates seem to have a better I-V performance. We are currently conducting further study to improve the performance of metallic glassy bipolar plates.

References

- [1] S. Yamaura, M. Yokoyama, H.M. Kimura and A. Inoue, J. Phys.:Conf. Ser. **144**, 012001 (2009).
- [2] M. Yokoyama, S. Yamaura, H.M. Kimura and A. Inoue, Int. J. Hydrogen Energy **33**, 5678 (2008).

Key Words

Metallic Glass, Bipolar Plate, Fuel Cell

Contact to

Shin-ichi Yamaura (NEDO Laboratory for Metallic Glass Research Collaboration and Promotion)
e-mail: yamaura@imr.tohoku.ac.jp

3DAP and Positron Annihilation Study of Precipitation Behavior in Cu-Cr-Zr Alloy

Precipitation behavior in a Cu-0.78%Cr-0.13%Zr alloy during aging and reaging has been studied by laser-assisted local electrode three-dimensional atom probe (Laser-LEAP) and positron annihilation spectroscopy (PAS). PAS experiments demonstrate the formation of vacancy-like defects and their association with Cr during the heat treatments.

Cu-Cr-Zr is considered as one of the candidate materials for the heat sink of the International Thermonuclear Experimental Reactor (ITER) divertor. Thermal aging is used to achieve high strength by precipitation hardening and simultaneously high thermal conductivity of Cu-Cr-Zr alloys. However, there has not been a unanimous conclusion on the microstructure of Cu-Cr-Zr. To clarify the precipitation behavior we have employed Laser-LEAP and positron annihilation spectroscopy (PAS).

The test specimens of Cu-0.78wt% Cr, 0.13wt% Zr, 0.003wt% Si, 0.008wt% Fe were solution annealed (SA) at 960°C for 3 h and then quenched, followed by prime aging at 460°C (PA) and reaging (overaging) at 600°C for 1 (RA1) and 4h (RA2), respectively [1].

Figure 1 shows atom maps around each Cr-rich precipitate in the PA and reaged states. In the precipitate of the PA state shown in Fig. 1 (a), Zr, Fe and Si impurities are found to be slightly segregated on the surrounding region of the Cr-rich core. In the RA1, 2 state, the Cr-rich precipitates coarsened as state above and the Zr, Si and Fe impurities furthermore segregated to form enriched layer regions as shown in Fig. 1 (b, c); the Cr-rich precipitates are covered by enriched regions.

Positron lifetime spectra of the alloy after the heat treatment were well described single lifetime components [2]; these lifetimes are longer than the positron lifetime of bulk Cu (110 ps) but shorter than that of monovacancies in Cu (173 ps). Thus, they are given by averaged positron lifetimes between the bulk and vacancy-like defects. Fig. 2 (a) shows the ratio curves of the coincidence Doppler broadening (CDB) spectra, normalized to that of pure Cu, of the heat treated Cu-Cr-Zr alloy together with those of pure Cr and Zr as references. Furthermore, that of neutron-irradiated Cu (C-80T) is also shown; its average positron lifetime is about 176 ps which exhibits that almost of all the positrons are trapped at irradiation-induced monovacancies. Small increases at the lower momentum regions accompanied sluggish decreases at higher momentum regions are seen for the curves of the SA and PA states. However, these changes in the ratio curves are markedly enhanced in the curves for the reaged states of RA1 and RA2, which means the introduction of ample vacancy-like defects by reaging and is consistent with positron lifetime observation stated above. To see the origin of the valley, the CDB spectrum of the RA1 is normalized to neutron-

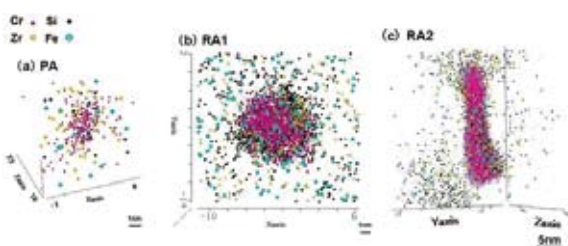


Fig. 1 Atom maps of the solute and impurity distributions in the Cu-Cr-Zr alloy with different heat treatments: (a) PA, (b) RA1 and (c) RA2.

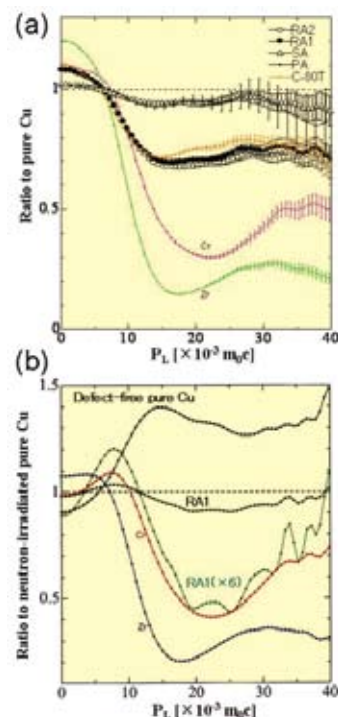


Fig. 2 Ratio curves of the CDB spectra for the Cu-Cr-Zr alloy. CDB spectra are normalized to defect free pure Cu (a) and neutron irradiated pure Cu (C-80T) (b).

irradiated pure Cu, together with that of pure Cr and Zr as shown in Fig. 2 (b). A broad valley centered around $20 \times 10^{-3} m_e c$ is observed. The ratio curve multiplied by a factor of 6 is found to be very close to that of pure Cr. This shows that about 1/6 (15%) of positrons annihilate with Cr electrons and the remaining 5/6 (85%) of positrons annihilate with Cu electrons. Furthermore, the fraction of positrons which annihilate with Cr electron, I_{Cr} , is estimated for the RA1 and RA2 states, using the fitting of high-momentum part of the CDB ratio curves: 15% for the RA1 and 17% for RA2, respectively. The above positron lifetime and CDB experiments demonstrate that more than 80% of positrons are trapped at vacancy-like defects induced by reaging and about 15% of them annihilate with surrounding Cr electrons in the reaged states. This suggests that the vacancy-like defects are induced in the interface regions between the Cr-rich precipitates and the Cu matrix in the reaged states.

References

- [1] M. Hatakeyama, T. Toyama, Y. Nagai, M. Hasegawa, M. Eldrup and B.N. Singh, Mater. Trans. 49, 518 (2008).
- [2] M. Hatakeyama, T. Toyama, J. Yang, Y. Nagai, M. Hasegawa, T. Ohkubo, M. Eldrup and B.N. Singh, J. Nucl. Mater. 386-388, 852 (2002).

Key Words

Future Energy/Environmental Materials, Cu-Cr-Zr, Precipitate

Contact to

Masahiko Hatakeyama (International Research Center for Nuclear Material Science)
e-mail: hatake@imr.tohoku.ac.jp

Variety of the Flux Pinning State Diagrams for Various c-axis Correlated Pinning Centers

In order to understand the flux pinning mechanism with the different variety of the c-axis-correlated disorder, the angular dependence of critical current density J_c was measured in detail for an Y123 film with BaZrO₃ nano-rods, a Sm123 film fabricated by the low temperature growth (LTG) technique and an Y123 film introduced the columnar defects by the heavy ion irradiation parallel to the c-axis. We found that the flux pinning state is similar in low fields below the matching field, but it shows different behaviors in high fields above the matching field for the variety of the c-axis correlated pinning. It is considered that the interstitial vortices interacted with the c-axis-correlated disorders through the vortex interaction may play an important role for the appearance of the c-axis-correlated pinning behavior in a high-field region above the matching field.

Practical high temperature superconducting (HTS) tapes and wires are developing under the national projects in the world. However one of the serious issues is the large anisotropy of the HTS materials. To overcome the large anisotropy of the superconducting parameters such as a critical current density J_c and an irreversibility field B_i , c-axis correlated pinning centers, i.e. columnar shaped precipitates or disorders along c-axis of the superconducting matrix, are introduced. Typical c-axis correlated pinning centers are the fission tracks by the heavy ion irradiation, dislocation and columnar-shaped precipitates along c-axis. It is considered that the flux pinning behaviors, which determine the J_c and B_i properties, are related to those density, size and growth directions. In order to clarify the detailed flux pinning behavior under the various c-axis correlated pinning centers, we measured the transport J_c in wide range of a temperature, a magnetic field and a magnetic field angle carefully and discuss the flux pinning behavior.

We selected three different RE_{1-x}Ba_{2-x}Cu₃O_y (RE: rare-earth) films with different c-axis correlated pinning centers such as the nano-scale BaZrO₃ columnar-shaped precipitates, i.e. nanorods (BZO-Y123), columnar defects by the irradiation of the Au-ions with 240 MeV (CD-Y123), and dislocations along c-axis (LTG-Sm123). Typically, the peak appears on the angular dependence of J_c for $\theta = 0^\circ$ (B//c), if c-axis correlated pinning works effectively. Hence, the c-axis correlated pinning state can be determined by the existence

of the J_c peak for B//c. Fig. 1 is the flux pinning state diagrams for three different films, which were determined by the angular dependence of J_c . In the orange-hatched region, the J_c (θ) peak for B//c can be observed, and then the c-axis correlated pinning behavior is dominant. On the other hand, in the yellow region, the random pinning is dominant because the J_c peak attributed to the c-axis correlated pinning vanishes. We can see the c-axis correlated pinning dominant region in low fields for all samples. However the pinning behaviors in a high field region are different among a sort of the c-axis correlated pinning [1]. It is suggested that the size and direction of the c-axis correlated pinning centers affect the flux pinning state.

According to the theory, the strong Bose glass state exists below the matching field [2]. Here, the matching field is a corresponding magnetic field estimated by the number of c-axis correlated pinning centers and a flux quantum. However it changes to the weak Bose glass state due to the existence of the interstitial vortices in between vortices pinned directly by the c-axis correlated disorders [3]. In this case, those interstitial vortices should interact with either the c-axis correlated disorders through the vortex interaction or the random pinning directly. Therefore, we have to consider the elastic behavior of the vortices under the competitive state between the random and the correlated pinning, in order to understand the complex vortex pinning state diagram.

References

- [1] M. Namba, S. Awaji, K. Watanabe, T. Nojima, S. Okayasu, M. Miura, Y. Ichino, Y. Yoshida, Y. Takai, T. Horide, P. Mele, K. Matsumoto, Appl. Phys. Exp. 1 (2008) 031703.
- [2] D. R. Nelson and V. M. Vinokur: Phys. Rev. B 48 (1993) 13060.
- [3] V. M. Pan and A. V. Pan: Low Temp. Phys. 27 (2001) 732.

Key Words

Superconductor, Critical Current Density, High Magnetic Field

Contact to

Satoshi Awaji (High Field Laboratory for Superconducting Materials)
e-mail: awaji@imr.tohoku.ac.jp

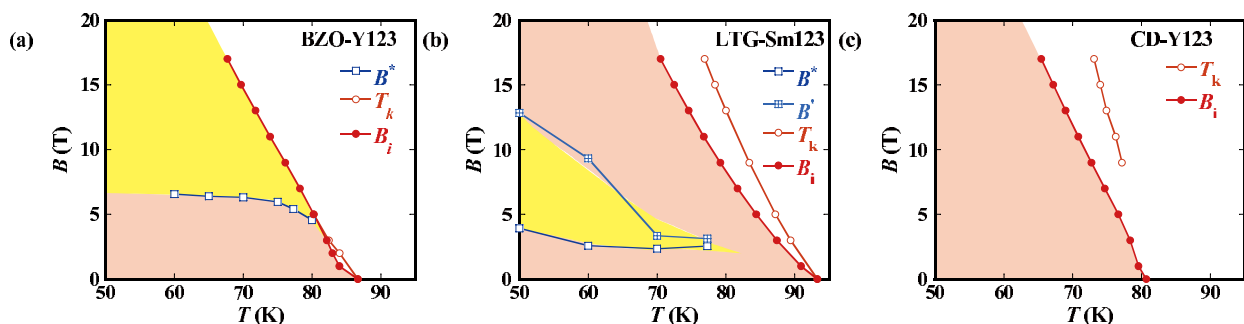


Fig. 1 Schematic flux pinning state diagrams at B//c for (a) BZO-Y123, (b) LTG-Sm123, and (c) CD-Y123. B^* , B' are the characteristic magnetic fields at which J_c peak for B//c vanishes and appears with increasing a magnetic field, respectively. B_i is the irreversibility field, T_k is an onset temperature of the pinned flux liquid state.